



---

Some Salient Features of the Time -Averaged Ground Vehicle Wake

Author(s): S. R. Ahmed, G. Ramm and G. Faltin

Source: *SAE Transactions*, Vol. 93, Section 2: 840222—840402 (1984), pp. 473-503

Published by: SAE International

Stable URL: <https://www.jstor.org/stable/44434262>

Accessed: 15-12-2018 11:01 UTC

---

JSTOR is a not-for-profit service that helps scholars, researchers, and students discover, use, and build upon a wide range of content in a trusted digital archive. We use information technology and tools to increase productivity and facilitate new forms of scholarship. For more information about JSTOR, please contact [support@jstor.org](mailto:support@jstor.org).

Your use of the JSTOR archive indicates your acceptance of the Terms & Conditions of Use, available at <https://about.jstor.org/terms>



JSTOR

*SAE International* is collaborating with JSTOR to digitize, preserve and extend access to *SAE Transactions*

# Some Salient Features of the Time -Averaged Ground Vehicle Wake

S. R. Ahmed and G. Ramm  
Institut für Entwurfs-Aerodynamik, DFVLR

G. Faltin  
Techn. Univ. Braunschweig

## Abstract

For a basic ground vehicle type of bluff body, the time averaged wake structure is analysed. At a model length based Reynolds number of 4.29 million, detailed pressure measurements, wake survey and force measurements were done in a wind tunnel. Some flow visualisation results were also obtained. Geometric parameter varied was base slant angle. A drag breakdown revealed that almost 85 % of body drag is pressure drag. Most of this drag is generated at the rear end.

Wake flow exhibits a triple deck system of horseshoe vortices. Strength, existence and merging of these vortices depend upon the base slant angle.

Characteristic features of the wake flow for the low drag and high drag configurations is described. Relevance of these phenomena to real ground vehicle flow is addressed.

2.473

0096-736X/85/9302-0473\$02.50

Copyright 1985 Society of Automotive Engineers, Inc.

## 1. Introduction

Ground vehicles can be termed as bluff bodies moving in close vicinity of the road surface. The shape of such vehicles evolved over the years under the constraints of aesthetics, operational safety, service accessibility etc. Effect of these design guidelines on aerodynamics was not of prime importance in the past.

With the increased concern about future availability of fuel, fuel economy is an important requirement expected of a modern car or utility vehicle. Fuel consumption depends, among other factors, on the aerodynamic drag of the vehicle.

A key feature of the flow field around a vehicle are the regions of separated flow. Even simple basic vehicle configurations free of all appendages and having smooth surfaces generate a variety of quasi two-dimensional and fully three-dimensional regions of separated flow. A major contribution to the drag of a vehicle stems from the pressure drag which is a consequence of flow separation.

In a time averaged sense, the regions of flow separation exhibit complex kinematic macro structures. Such structures in the wake, which is the major separated flow region of a vehicle flow field, determine the drag experienced by the body.

A qualitative understanding of the flow phenomena in bluff body wakes is available in aeronautical and automotive literature. Results which could enhance the quantitative insight into the complex interrelation between wake structure, pressure distribution on body surface, drag and configuration geometry are scarce. Lack of this information is a major hinderance to the attempts currently being undertaken to theoretically model vehicle flow fields. This data can also be used to validate the computational codes developed.

Based on extensive experimental results, this paper attempts to (1) identify the time-averaged flow structures present in the wake of a basic vehicle type body, and (2) analyse the effect of body geometry on wake structure, pressure distribution and drag. Attention is focussed on rear end geometry and wake structure. This was the consequence of a drag breakdown analysis, which indicated that

most of the drag is generated by flow mechanisms at the body rear end.

## 2. Experimental investigations

### Model

Selection of the configuration used in this study was governed by the requirement that it should generate the essential features of a real vehicle flow field, with the exception of that due to rotating wheels, engine and passenger compartment flow, rough underside and surface projections. It was conjectured that the model chosen should generate: a strong three-dimensional displacement flow in front, relatively uniform flow in the middle, and a large structured wake at the rear.

The wind tunnel model, Fig. 1, with an overall length of 1.044 m had a length : width : height ratio of 3.36 : 1.37 : 1. It consisted of three parts; a fore body, a mid section and a rear end. Edges of the fore body were rounded, as indicated in Fig. 1, to achieve a separation free flow over its surface. Middle section was a box shaped sharp edged body with a rectangular cross section. A set of nine interchangeable rear ends enable a base slant variation in steps of  $5^\circ$ , between the value of  $0^\circ$  and  $40^\circ$ . A tenth rear end variant, with  $12.5^\circ$  base slant was also tested. All rear ends had same base slant length  $l_s$  of 222 mm and had sharp edges. Morel [1] used a similar bluff body to investigate the effect of base slant on drag behaviour.

One half of the model was instrumented with pressure taps. A total of 210 taps on the fore body and 83 taps on the mid section were evenly distributed on the surface. Only three rear ends with slant angles of  $5^\circ$ ,  $12.5^\circ$  and  $30^\circ$  were equipped with pressure taps. The  $5^\circ$ -rear end had 444, the  $12.5^\circ$ -rear end 430 and the  $30^\circ$ -rear end 450 pressure holes distributed evenly over one half of its surface. Scanivalves for acquisition of pressure data were installed inside the model body.

### Wind tunnel and test set-up

The tests were conducted in the DFVLR subsonic wind tunnels at Braunschweig (pressure measurements, flow visualization) and

Göttingen (wake survey, force measurements). These facilities, described in [2] and [3] are open test section, closed return, wind tunnels with a square 3 m by 3 m nozzle. A test section length of about 5.8 m is available for the experimental set-up.

The model was fixed on cylindrical stilts 50 mm above a ground board 3 m wide and 5 m long, Fig. 2. About 1.35 model length of ground plane projected in front and 2.43 model length behind the model. Leading edge of ground board was carefully rounded to avoid any separations.

All tests, except the flow visualization, were performed at a wind speed of 60 m/s. This corresponds to a model length based Reynolds number of 4.29 million. In both tunnels the turbulence intensity lies below 0.5 per cent.

#### Wake survey

A ten hole directional probe, Fig. 3, which is a further development of the probe used in earlier experiments [4], [5], [6], was employed for the wake survey. On the conical tip of the yawmeter probe, two pairs of opposing orifices are arranged. One pair is sensitive primarily to flow yaw and the other to flow incidence. To determine the flow angularity, yaw rotations are imposed on the probe till the pressure in the yaw sensing orifice pair is equalised. In this position, the probe tip axis is pointing nominally along the direction of local flow yaw. Local flow incidence is computed from the pressure difference of the incidence-sensitive orifice pair via a calibration curve. In the yaw mode, the probe shaft is vertical.

Alternately, with probe shaft horizontal, incidence rotations can be imposed to equalise the pressure in incidence sensing orifice pair. Yaw angle is determined then, as before, with a calibration curve. The decision, which orifice pair is used to align the probe tip depends upon the anticipated incidence and yaw gradients in the flow.

Mean value of the pressure sensed by the four orifices on the cylindrical sleeve of probe tip, and the pressure in the tip

orifice are functions of local static and total pressure. Calibration curves are used to evaluate the static and dynamic pressure from this data. Thus magnitude and direction of local velocity vector are determined.

The tenth orifice, situated at the probe tip rear ( $p_{Rev.}$  in Fig. 3), is used to detect flow reversal. If the total pressure measured here exceeds the value sensed at the probe tip, the probe shaft is rotated  $180^\circ$ . Nomenclature and formulae for evaluating the flow and velocity components from probe data are summarised in Fig. 3.

The wake survey probe was mounted on a rigid carriage which provides cartesian translation along the full length, width and height of the test section. Such movements are remote controlled and digitized by electronic counters. A wake scan in a  $y_A$ - $z_A$  plane is performed by moving the probe in  $z_A$  direction with  $x_A$  and  $y_A$  positions kept fixed. The  $z_A$ -traverse was repeated with a new value of  $y_A$  which was stepwise increased. During the  $z_A$ -traverse, the probe halted at discrete points for a duration of 2s. The analog values recorded during this period were integrated and were used to compute the mean pressure values.

Estimated accuracy of flow angle measurement is  $\pm 0.4^\circ$ . Errors of upto 1 per cent of free stream dynamic pressure are present in the pressures measured. More details of the accuracy estimates are given in [5].

#### Pressure and force measurements

Pressure and force measurement results reported here are restricted to the zero yaw onset flow condition. Some experiments conducted with yawed onset flow in the range of  $\beta = \pm 10^\circ$  served mainly as a check of the flow symmetry.

For force measurements, the model was connected to a strain gauge balance, arranged below the ground plane, by four cylindrical stilts. Balance assembly was screened from tunnel air flow by a casing.

Estimated errors in the force and moment measurements are  $\pm 0.2$  N and  $\pm 0.1$  Nm respectively.

### 3. Experimental Results

#### Drag and pressure measurements

Variation of drag  $c_W$  with base slant angle  $\varphi$ , for a body of the type studied here has been already reported by Morel [1]. Also Janssen and Hucho [7], in an earlier paper, described a similar drag behaviour for a passenger car. Fig. 4 illustrates the drag breakdown obtained through force and pressure measurements for the zero yaw onset flow conditions. Even though apparent differences were present in the model geometry (edge radii, overall dimensions, stilt positions etc.) and a different ground clearance was used in the test setup, the total drag values obtained are almost same to those of Morel [1].

Contributions to pressure drag from front part  $c_K^*$ , slant rear end  $c_S^*$ , and vertical rear end base  $c_B^*$  were evaluated by integration of the axial component of the measured pressure over the surface. Basis for drag breakdown are pressure measurements on configurations with rear end slant angles  $\varphi$  of  $5^\circ$ ,  $12.5^\circ$  and  $30^\circ$ . The low drag flow for  $\varphi = 30^\circ$  was realised by fixing a splitter plate vertically on the ground board in the plane of symmetry behind the model. Between the upstream edge of the splitter plate and the model base, a gap of about 25 mm was left free.

Numerical values of the drag contributions are given in Table 1 below. Total drag value has been corrected for tare drag of stilts.

Base slant angle $\varphi$	$c_W$	$c_K^*$	$c_S^*$	$c_B^*$
$5^\circ$	0.231	0.016	0.010	0.158
$12.5^\circ$	0.230	0.016	0.037	0.122
$30^\circ$ (High Drag)	0.378	0.016	0.213	0.092
$30^\circ$ (Low Drag)	0.260	0.019	0.089	0.101

Table 1. Drag breakdown for three configurations

Results of Fig. 4 and Table 1 clearly demonstrate the small contribution of forebody to the total pressure drag. For the

configuration studied, its value remains, (except for the 30° base slant low drag situation), constant at  $c_K^* = 0.016$ . A conclusion, which can be drawn from this is that the interference between the rear end and fore body flow is weak; this could be a consequence of the relatively long mid section. The result is not necessarily valid for configuration with a short mid section. As the flow leaving the fore body feeds the flow on the mid and aft sections of the body, and subsonic flow is considered, interference between upstream and downstream flow regions is to be anticipated.

Major contribution to the pressure drag comes from the slant and vertical base surface of rear end. For base slant angle  $\varphi = 0^\circ$ , rear end pressure drag is wholly contributed by the flat base; with increasing values of  $\varphi$ , the vertical base area decreases, but the pressure distribution is changed as well, see Table 2. Thus there are two overlapping effects, one geometrical, the other fluid mechanical.

$\varphi$	Total Pressure Drag $c_P^* = c_K^* + c_S^* + c_B^*$	Vertical Base		Slant Surface		Fore-body $c_K^*/c_P^*$	$\frac{c_P^*}{c_W}$	$\frac{c_R^*}{c_W}$
		Base Area/ Front Area	$c_B^*/c_P^*$	Projected Area/ Front Area	$c_S^*/c_P^*$			
5°	0.184	0.933	0.86	0.07	0.054	0.087	0.800	0.200
12.5°	0.175	0.833	0.70	0.17	0.211	0.091	0.757	0.243
30° (High Drag)	0.321	0.615	0.29	0.39	0.664	0.050	0.849	0.151
30° (Low Drag)	0.209	0.615	0.48	0.39	0.426	0.091	0.804	0.196

Table 2. Relative Drag Contributions

With  $\varphi$  changing from 5° to 30° (see Table 2), the vertical base area decreases from 93 % of front area to 61.5 %; the  $c_B^*$  value decreases from 86 % to 29 % of total pressure drag. For the same  $\varphi$  variation, the projected area of slant surface increases from 7 % to 38.5 % of model front area; the contribution to pressure drag  $c_S^*$  increases thereby from 5.4 % to 66.4 %. These figures emphasize that the pressure drag for the basic body considered here is mainly generated on the slant and vertical base of the rear end.

Also shown in Table 2 are the relative magnitudes of the total

pressure drag  $c_p^*$  and friction drag  $c_R^*$  referred to the overall drag  $c_W$ . The relative values of pressure drag vary between 76 % to 85 %, with friction drag accounting for the rest of 24 % to 15 %. Considering the "minimum" drag configuration with  $\varphi = 12.5^\circ$ , 76 % of its total drag is pressure drag and the rest 24 % friction drag. The high drag configuration with  $\varphi = 30^\circ$  has 85 % of its total drag resulting from pressure drag, with the rest 15 % coming from friction drag. Contribution of friction drag to the overall drag becomes thus of increasing importance for low drag configurations.

Fig. 5 shows the static pressure isobars on the unfolded rear end surface. Presence of vortices at side edges of the slant surface is visible for the configurations  $\varphi = 12.5^\circ$  and  $30^\circ$  (high drag condition).

Except in the vicinity of the side edges, the flow on the slant surface of  $\varphi = 12.5^\circ$  configuration appears to be "two dimensional". This is evident from the parallel isobars running across the surface. A large portion of the flow coming off the upstream edge of this surface, experiences a pressure recovery, which results in the low values of  $c_S^*$  and  $c_B^*$  (see Table 1). Strong vortices are present in the flow field of  $\varphi = 30^\circ$  configuration experiencing a high drag, Fig. 5. The vortices influence and shape the flow over the whole slant surface. Low drag flow for this configuration shows a flow separation at the slant surface upstream edge.

The usual assumption of a constant base pressure is not confirmed by the results of Fig. 5. Especially for the  $\varphi = 30^\circ$  configuration, the pressure on base is influenced by flow on slant and undersurface.

### Wake structure

Even though the wake flow of a bluff body is basically unsteady, the time averaged flow exhibits a macrostructure which appears to govern the pressure drag created at the rear end. Before discussing the quantitative results of the wake survey, the salient flow features of the wake, deduced from these results, are

illustrated in Fig. 6. This schematic sketch of the flow phenomena is the result of present and earlier studies [4], [5], [6]. The shear layer, coming off the slant side edge, rolls up into a longitudinal vortex, in a manner similar to that observed on side edge of low aspect ratio wings. At the top and bottom edges of the flat vertical base, the shear layer rolls up as indicated, into two recirculatory flow regions A and B, situated one over another. The flow on the base surface, derived from oil flow pictures, does not indicate that the flow regions A and B end on the base surface. Consequently the recirculatory flow A and B can be thought of as being generated through two "horseshoe" vortices situated one above another in the "separation bubble" indicated by D in Fig. 6. The "bound" legs of these vortices are approximately parallel to the base surface; the "trailing" leg of upper vortex A, aligns itself in direction of onset flow and merges with the vortex C coming off the slant side edge. Downstream development or dissipation of the lower vortex B has been difficult to analyse during the present and previous investigations, so that a conclusive statement about its behaviour cannot be made. The shear layer separating at the vertical side edges of the base seems to split up, part of it drawn upwards into the "trailing" leg of vortex A and into vortex C; rest of it probably merges into the "trailing" leg of vortex B. Streamlines on base surface, schematically shown in Fig. 6, indicate this process.

As the flow over the slant surface is influenced by the vortex C coming off the side edge, the strength of vortex A is dependent upon the strength of vortex C. As long as flow remains attached over the slant surface, strength of vortex C depends upon the base slant angle  $\varphi$ ; consequently the strength of vortex A also depends upon the angle  $\varphi$ . Strength of vortex B depends in the first instance upon the flow conditions in the ground clearance gap. It is indirectly linked to the base slant angle  $\varphi$  over the vortices A and C.

Quantitative data to support the flow module described above is presented in Figs. 7,8 and 9. For the base slant angles of  $\varphi = 5^\circ$

and  $25^\circ$ , the distribution of the velocity vector  $V_{xz}$  in the plane of symmetry of the wake is shown in Fig. 7<sup>\*\*</sup>. The length of the pointers equals the magnitude of velocity vector  $V_{xz}$  at the location considered.

Clearly visible are the recirculatory flows A and B of Fig. 6. Also the separation bubble boundary D can be identified. Flow velocities near the model base and in the region where the separation bubble "closes" are small and difficult to measure; the blank regions indicate the area where meaningful results could not be obtained by the probe.

Fig. 7 illustrates also the change effected in the extent of the recirculating flows in wake due to a change in the base slant angle. Where as for  $\varphi = 5^\circ$ , both the upper and lower regions are of comparable order of magnitude, with  $\varphi$  increased to  $25^\circ$ , the upper region dominates the flow phenomena in the wake. Also the length of the separation bubble is almost halved.

A plot of the velocity vector  $V_{yz}$  in a transverse plane close to the model base is shown in Fig. 8 for the  $\varphi = 5^\circ$  configuration. This result is in support of the concept of two horseshoe vortices in the wake as hypothesized above.

The merging process of the upper horseshoe vortex A (see Fig. 6) with the vortex C coming off the side edge is depicted in the results of Fig. 9. Shown are the velocity distributions in the one half of the symmetric transverse planes at  $x_A/l = -0.077$ ,  $-0.19$  and  $-0.479$  for the  $\varphi = 25^\circ$  configuration\*. The cross section boundary of the bubble is shown shaded in Figs. 9 a and b. The contour of the bubble edge was evaluated by assuming it to be situated at points where the total pressure coefficient  $c_p$  equals 0.1. Region of reversed flow, is cross hatched.

Formation of the side vortex is clearly visible in Fig. 9 a; it is also seen that its core is fed by the separation bubble. Velocity vectors in the cross hatched region indicate the existence of an upper and lower region of reversed flow; the axis of the upper

\* \_\_\_\_\_  
Wake survey results for  $\varphi = 30^\circ$  configuration were difficult to obtain as the high drag creating flow could not be maintained over a long period of time in wind tunnel tests.

\*\* \_\_\_\_\_  
Note the difference in scale of the velocity vectors plotted.

region is curved upwards in direction of the core of side edge vortex. Further downstream, at  $x_A/l = -0.19$ , the separation bubble narrows down, and the side edge vortex core, isolated, lies above the separation bubble "boundary".

Merging of side edge vortex and upper separation bubble vortex takes place close to the model base; after it, the edge vortex and separation bubble appear as separate entities; this seems to be the case especially where a strong side edge vortex is generated, as in the configuration with  $\varphi = 25^\circ$ . Still further downstream, at  $x_A/l = -0.479$ , the separation bubble closes, and the overall flow is dominated by the downwash inducing vortex, Fig. 9 c.

Fig. 10 illustrates schematically the features analysed for the high drag flow situation on the  $\varphi = 30^\circ$  rear end. For this base slant configuration, the flow in the middle part of the slant surface separates at the upstream edge; the presence of strong side edge vortices prevents a lateral widening of this separated flow. A closed, half elliptic region of circulatory flow "E", flanked by 2 triangular attached flow regions "F", is present on the slant surface. This may be assumed to be generated by a fourth vortex, whose axis is aligned with the core of the circulatory flow E in Fig. 10. The "trailing" leg of this vortex merges with the vortex coming off the side edge at the leading edge/side edge junction. Thus the core of the side edge vortex is fed with low energy material from the separated flow region on the slant base surface.

The presence of this separation region lowers the level of pressure prevalent on the complete surface of base slant; this contributes to the dramatic rise of the pressure drag evidenced by the results of Fig. 4, Table 1, and the isobar plots of Fig. 5.

Actually, the flow separation, in the region denoted by E in Fig. 10, is already initiated at still lower values of  $\varphi$ . This is shown in the oil flow picture series of Fig. 11. Formation of side edge vortex with a primary and secondary vortex formation can also be observed. Configurations with base slant angles slightly less than  $30^\circ$ , appear to generate the three individual vortices A, B and E of Figs. 6 and 10. With  $\varphi$  slightly above  $30^\circ$ , the separation region on the slant surface joins the separation bubble of the base, so

that the vortices A and E can no longer be considered as separate. This merging of the separation regions, probably triggered by seemingly insignificant disturbances in the oncoming flow, results in the switch over to the low drag type of flow in case of the  $\varphi = 30^\circ$  configuration. This low drag flow is characterised by the absence of the strong side edge vortices. Proof of this is shown in the total pressure isobar contours of Fig. 12. The pressure measurement was done at  $x_A = 0$ , i.e. at the base, just above the slant surface downstream edge.

In Fig. 12 a, the side edge vortex and the region of separated flow in the middle are clearly noticeable. The flow observed is that for a  $\varphi = 30^\circ$  configuration under high drag condition. Fig. 12 b illustrates the isobar contour for the low drag situation. Only a weak trend of the flow to turn around the side edge can be detected. Otherwise the flow appears to be separated over the complete slant surface.

In spite of the absence of the side edge vortices, which as discussed above shape the flow mechanisms in the wake, a similar cross flow field was observed in the far field for both flow situations, as shown in Fig. 13.

In the velocity distribution shown for the high drag flow (at the station  $x_A/l = -0.479$ ), a strong downwash creating vortex with a narrow core is to be seen, Fig. 13 a. In the low drag flow (Fig. 13 b), the roll up process of the shear layer coming off the rear end periphery is not yet complete. The reason that also in this case, a weaker but still downwash creating circulatory flow is generated, seems to be the following: the flow separating at the upstream edge of the slant surface induces a downward tilt to the oncoming flow off the upper surface. Flow coming off the side and lower edges of the rear end separates farther downstream, so that a downwards and inwards (from slant edge) tendency is imparted to the flow coming off the rear end.

Relevance of the flow phenomena described for the wake structure and drag behaviour of the idealized vehicle type body studied here for a real vehicle can be judged by comparing the present results with some results obtained earlier [6] on a quarter scale vehicle

model, having same overall dimensions. With the help of interchangeable upper rear ends, the base slant angle was varied systematically over the same range as in the present tests. Also the length of the base slant in plane of symmetry was same and equal to 222 mm. The plan form of the slant surface, however, changed with the base slant angle  $\varphi$ , as the model used in [6] had a curved side and roof surface. Another important difference to the present model was that the rear part of model undersurface was slightly upswept, creating a diffuser type of flow in the gap between model undersurface and ground board.

Fig. 14 shows photographic evidence, taken from [6], of the two recirculatory flow regions discussed above and denoted with A and B in Fig. 6. A thin smoke tube was projected vertically through the ground plane in the wake region, just below and above the separation bubble edge.

Drag results obtained for the model in [6], shown in Fig. 15 e confirm the trend indicated by the present results. Also the high drag value for both models is obtained at the same base angle of  $\varphi = 30^\circ$ .

Effect of undersurface upsweep has a similar influence on the wake development, as a base slant. A base slant imparts a downwards and inwards trend to the separating shear layer at top. An undersurface upsweep, imparts in a similar fashion, an upwards and inwards trend to the flow coming from beneath the vehicle. If the upsweep effect dominates, the longitudinal vortices created downstream have a rotation sense which generates an upwash. Fig. 14 a and d depict the situation where either the undersurface upsweep or the base slant dictates the final sense of rotation of the vortices in the wake. The cross over point, where a change in the sense of rotation takes place, lies between the base slant values of  $\varphi = 10^\circ$  and  $15^\circ$ . For this "optimum" value, the clearly defined vortex motion seen to be present at  $\varphi$ -values of  $5^\circ$  and  $25^\circ$  breaks down. The cross flow present at the "optimum" base slant angle is consequently anticipated to be weak. This phenomena is apparently associated with the aerodynamic drag; result of Fig. 14 e show that the drag value is lowest at a base slant angle of  $12.5^\circ$ .

Coming back to the wake flow module hypothesized in Fig. 6, the observations made above, lead to the following explanation. For the optimum low drag configuration, the strength of both horseshoe vortices A and B becomes equal. This can lead to a merging process, resulting in a ring of vortex, housed in the separation bubble emanating at the base. The weaker side edge vortex, appears to develop uninhibited by the flow phenomena inside the separation bubble. As the mutual strengthening of vortices A and C through merging is absent, the resulting cross flow in the downstream also weakens.

A result to substantiate the ring vortex formation concept, described above, is given in Fig. 16. In Fig. 16 a, the cross flow velocity vectors  $V_{yz}$ , and in Fig. 16 b the total pressure isobars at a downstream station  $x_A/l = -0.11$  are shown. Region of reverse flow is represented by a cross hatch. Referred to the vertical base area, the upper and lower regions of reverse flow are approximately equal in magnitude.

#### 4. Conclusions

1. For the basic bluff vehicle type of body considered, upto 85% of the total drag is pressure drag. Rest is friction drag.
2. With attached flow prevalent over its surface, the forebody contributes a maximum of 9% to the pressure drag. Rest of the pressure drag is generated at the rear end.
3. The time-averaged structure of the wake exhibits a pair of horseshoe vortices, situated one above another in the separation bubble at the vehicle base. Vortices, coming off the slant side edges are also present.
4. Strength of side edge vortices and the horseshoe vortices in the separation bubble is mainly determined by base slant angle.
5. A low drag rear end configuration induces a weak transverse flow in its wake.
6. High drag generating flow is characterized by strong side edge vortices, a separation bubble on the base slant surface, and

the separation bubble emanating from the vertical rear end base.

7. High drag flow, described under point 6 above, is unstable; the switch over to the stable low drag flow is accompanied by disappearance of strong vertical motion in the wake.

#### 5. Acknowledgement

The authors wish to thank Deutsche Forschungs- und Versuchsanstalt für Luft- und Raumfahrt (DFVLR) for the permission to publish this paper. They are indebted to the staff of the DFVLR wind tunnel department at Braunschweig and Göttingen for the cooperation and help offered.

#### 6. References

- [1] T. Morel: The Effect of Base Slant on the Flow Pattern and Drag of three-dimensional Bodies with Blunt Ends. Proceedings of Symposium on Aerodynamic Drag Mechanisms of Bluff Bodies and Road Vehicles, (Editors G. Sovran et al.), Plenum Press, New York, 1978, pp. 191 - 226.
- [2] H. Trienes: Der Normalwindkanal der Deutschen Versuchsanstalt für Luft- und Raumfahrt (DFL) in Braunschweig. Zeitschrift für Flugwissenschaften, 12 (1964), 4, pp. 135 - 142
- [3] F.W. Riegels, W. Wuest: Der 3-m Windkanal der Aerodynamischen Versuchsanstalt Göttingen. Zeitschrift für Flugwissenschaften, 9 (1961), pp. 222 - 228
- [4] S.R. Ahmed, W. Baumert: The Structure of Wake Flow Behind Road Vehicles. Symposium on Aerodynamics of Transportation, (Editors T. Morel et al.), ASME, New York, 1979, pp. 93 - 103
- [5] S.R. Ahmed: Wake Structure of Typical Automobile Shapes. ASME Journal of Fluids Engineering, Vol. 103, 1981, pp. 162 - 169
- [6] S.R. Ahmed: Influence of Base Slant on Wake Structure and Drag of Road Vehicles. ASME Journal of Fluids Engineering, Vol. 105, 1983, pp. 429 - 434

[7] W.-H. Hucho: The Aerodynamic Drag of Cars. Current Understanding, Unresolved Problems and Future Prospects. Symposium Proceedings, ref. [1], pp. 7 - 40

## 7. Nomenclature

b	model width ( = 389 mm)
$c_B^*$	vertical base pressure drag coefficient, based on F and $q_\infty$ (Fig. 4)
$c_G = (P_T - P_\infty) / q_\infty$	total pressure coefficient
$c_K^*$	forebody pressure drag coefficient, based on F and $q_\infty$ (Fig. 4)
$c_P = (P - P_\infty) / q_\infty$	static pressure coefficient
$c_R^*$	friction drag coefficient based on F and $q_\infty$
$c_S^*$	slant surface pressure drag coefficient, based on F and $q_\infty$ (Fig. 4)
$c_W = W / (q_\infty F)$	drag coefficient
F	projected frontal area of model
h, $h^*$	model height ( = 288 mm) and height above ground
l	model length ( = 1044 mm)
$l_S$	base slant length ( = 222 mm), Fig. 1
P, $P_\infty$	local and free stream static pressure
$P_T$	local total pressure
$q_\infty = \frac{\rho}{2} V_\infty^2$	free stream dynamic pressure
$V_{XA}, V_{YA}, V_{ZA}$	velocity components in $X_A, Y_A$ and $Z_A$ directions, (Fig. 3)
$V_{XZ}, V_{YZ}$	resultant of $V_{XA}, V_{ZA}$ or $V_{YA}, V_{ZA}$ velocity components

- $V_\infty$  free stream velocity
- $W$  drag force
- $X_A, Y_A, Z_A$  cartesian coordinates defined in Fig. 6
- $\alpha, \beta$  flow angles, defined in Fig. 3
- $\rho$  density
- $\varphi$  base slant angle

8. Illustrations

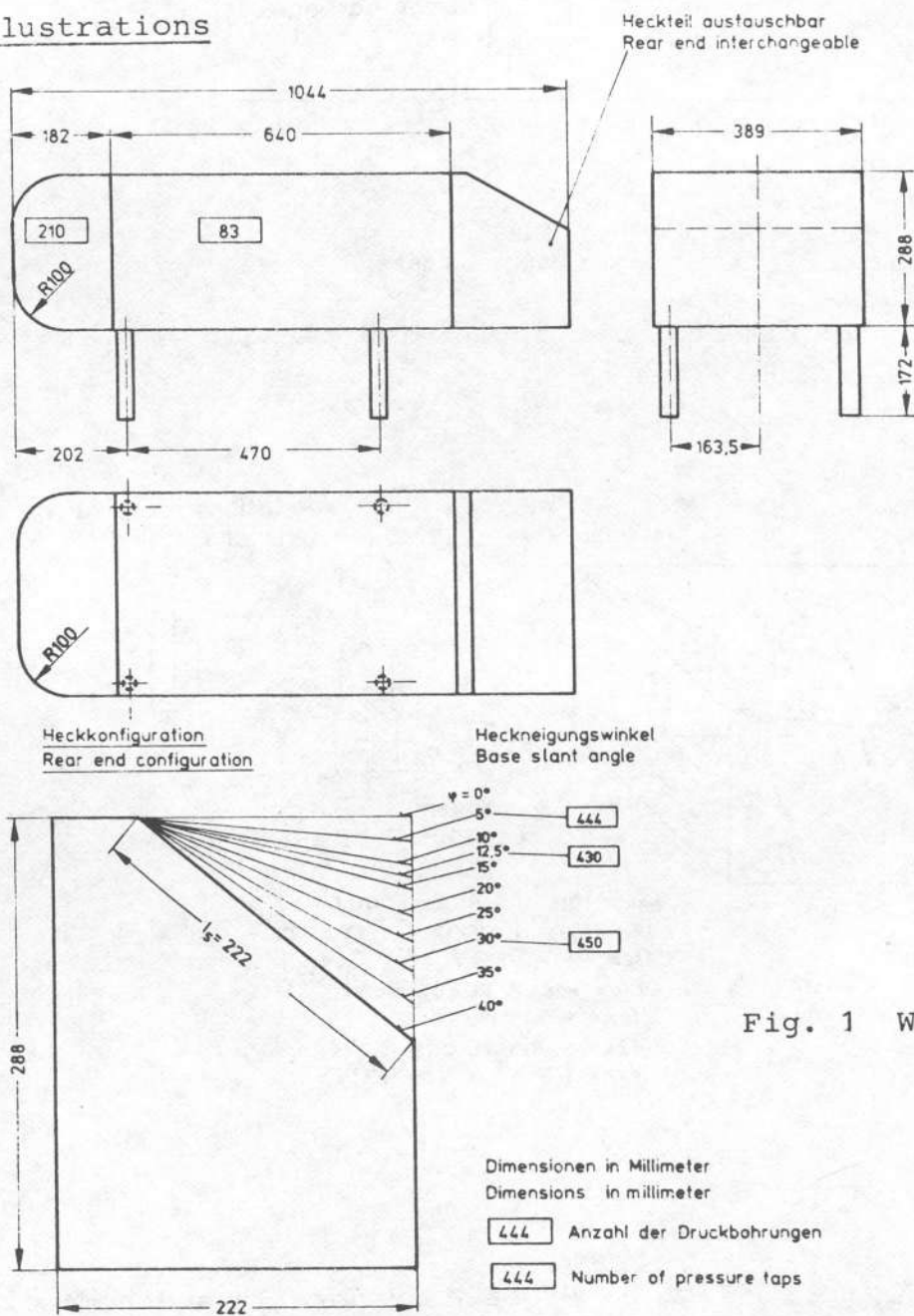


Fig. 1 Wind tunnel model

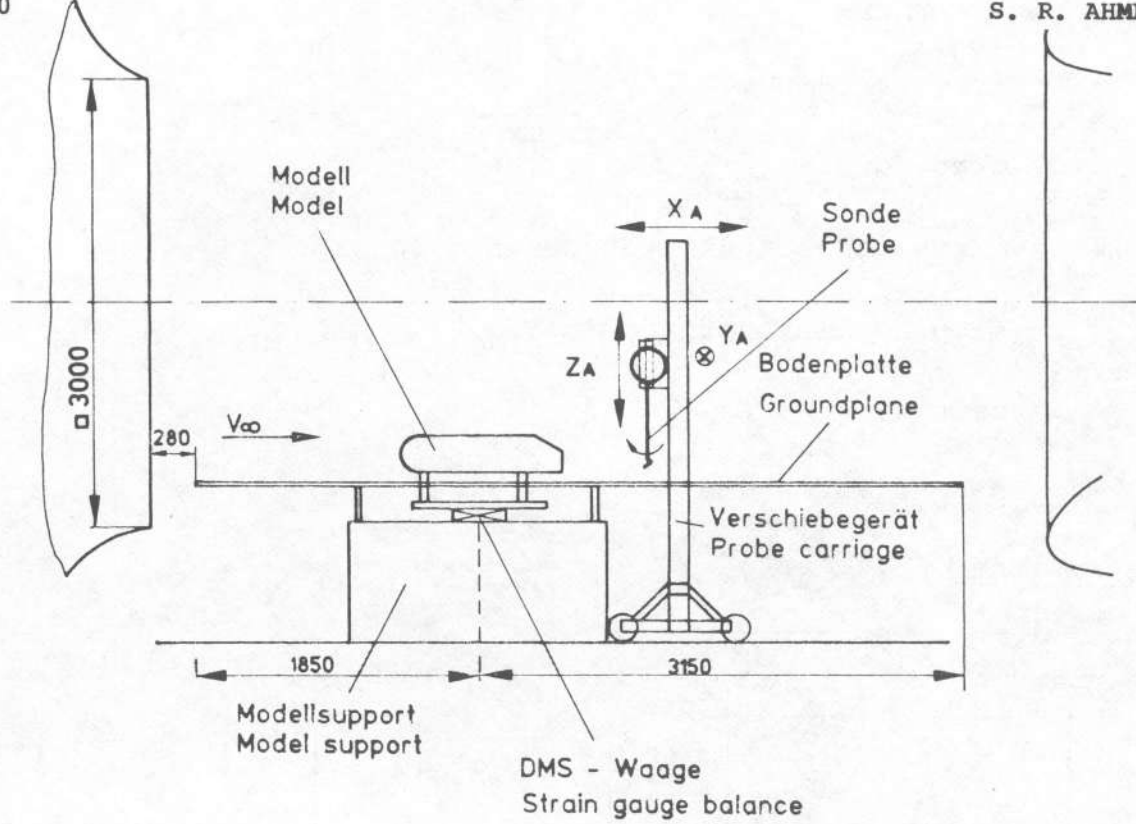
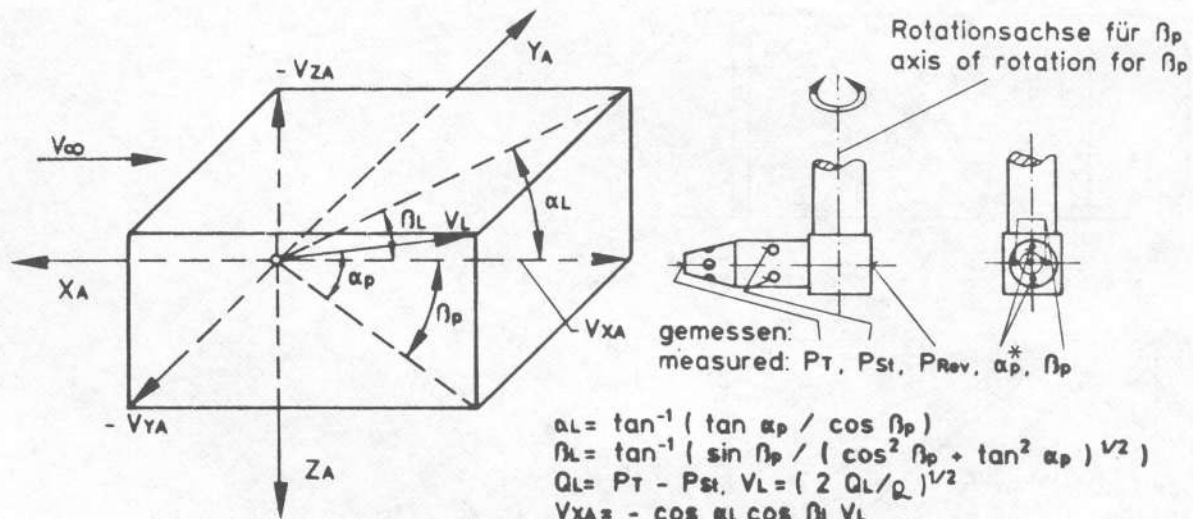


Fig. 2 Experimental set-up in wind tunnel



$$\alpha_L = \tan^{-1} (\tan \alpha_p / \cos \beta_p)$$

$$\beta_L = \tan^{-1} (\sin \beta_p / (\cos^2 \beta_p + \tan^2 \alpha_p)^{1/2})$$

$$Q_L = P_T - P_{St}, V_L = (2 Q_L / \rho)^{1/2}$$

$$V_{XA} = -\cos \alpha_L \cos \beta_L V_L$$

$$V_{YA} = -\sin \beta_L V_L$$

$$V_{ZA} = -\sin \alpha_L \cos \beta_L V_L$$

$$V_{YZ} = (V_{YA}^2 + V_{ZA}^2)^{1/2}$$

- Index L örtliche Werte  
local values
- P Sonde  
probe
- T gesamt  
total
- St statisch  
static
- Rev hinten  
revers
- \*  $\alpha_p$  aus Kalibrierkurve  
from calibration curve

Fig. 3 Probe head details and nomenclature

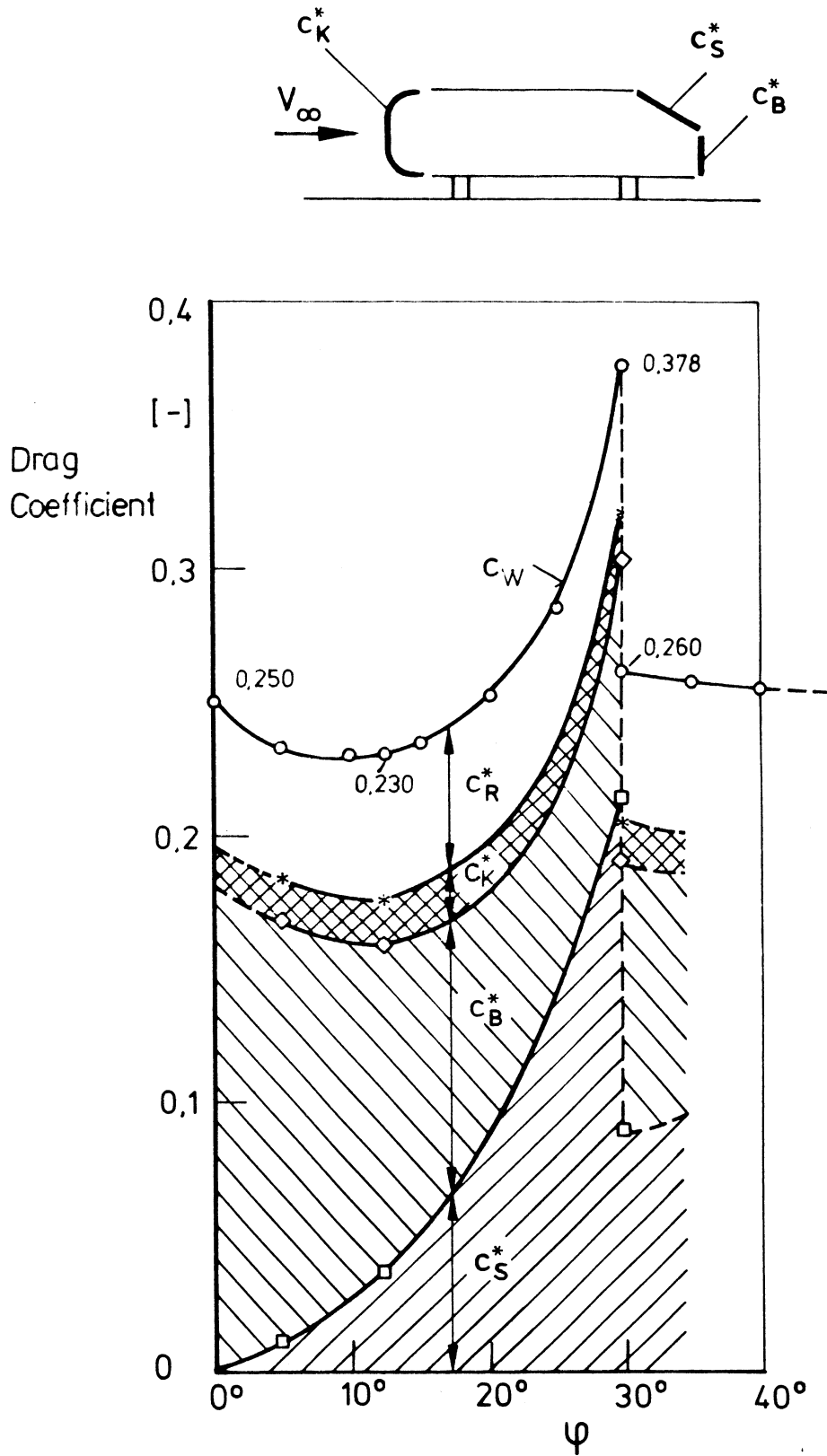


Fig. 4 Variation of Drag with base slant angle

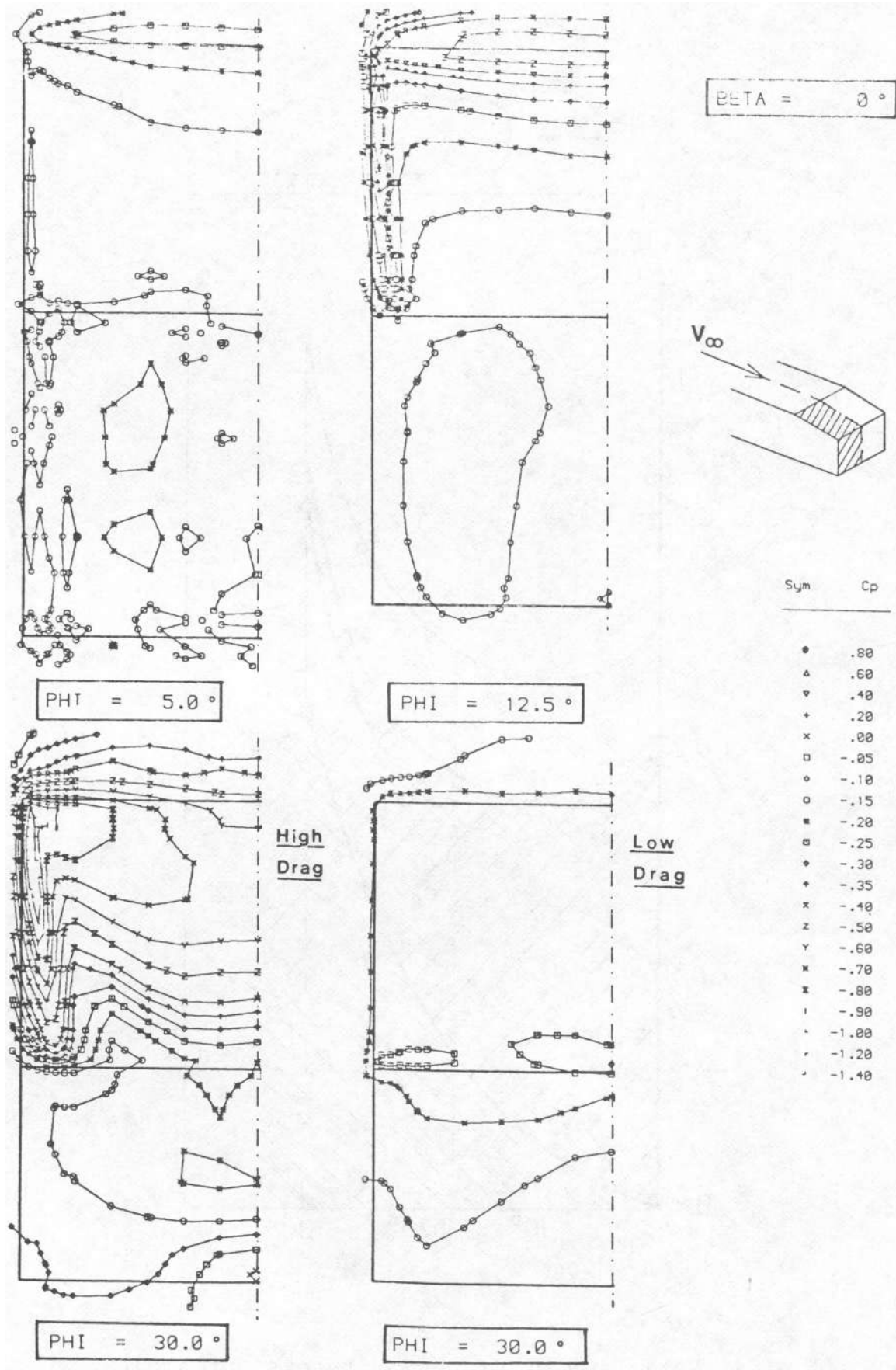


Fig. 5 Static pressure isobars on rear end surface

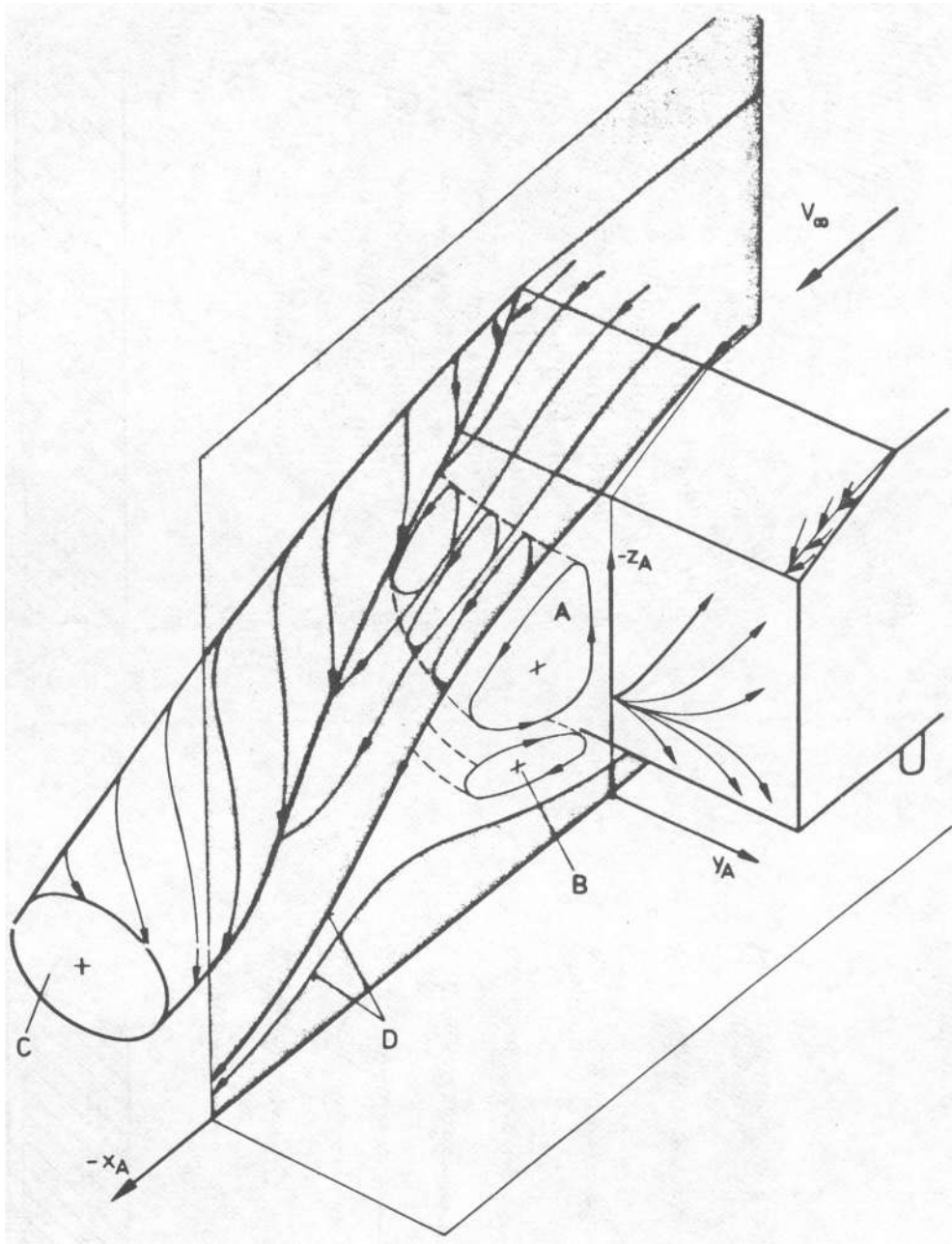


Fig. 6 Horseshoe vortex system in wake (schematic)

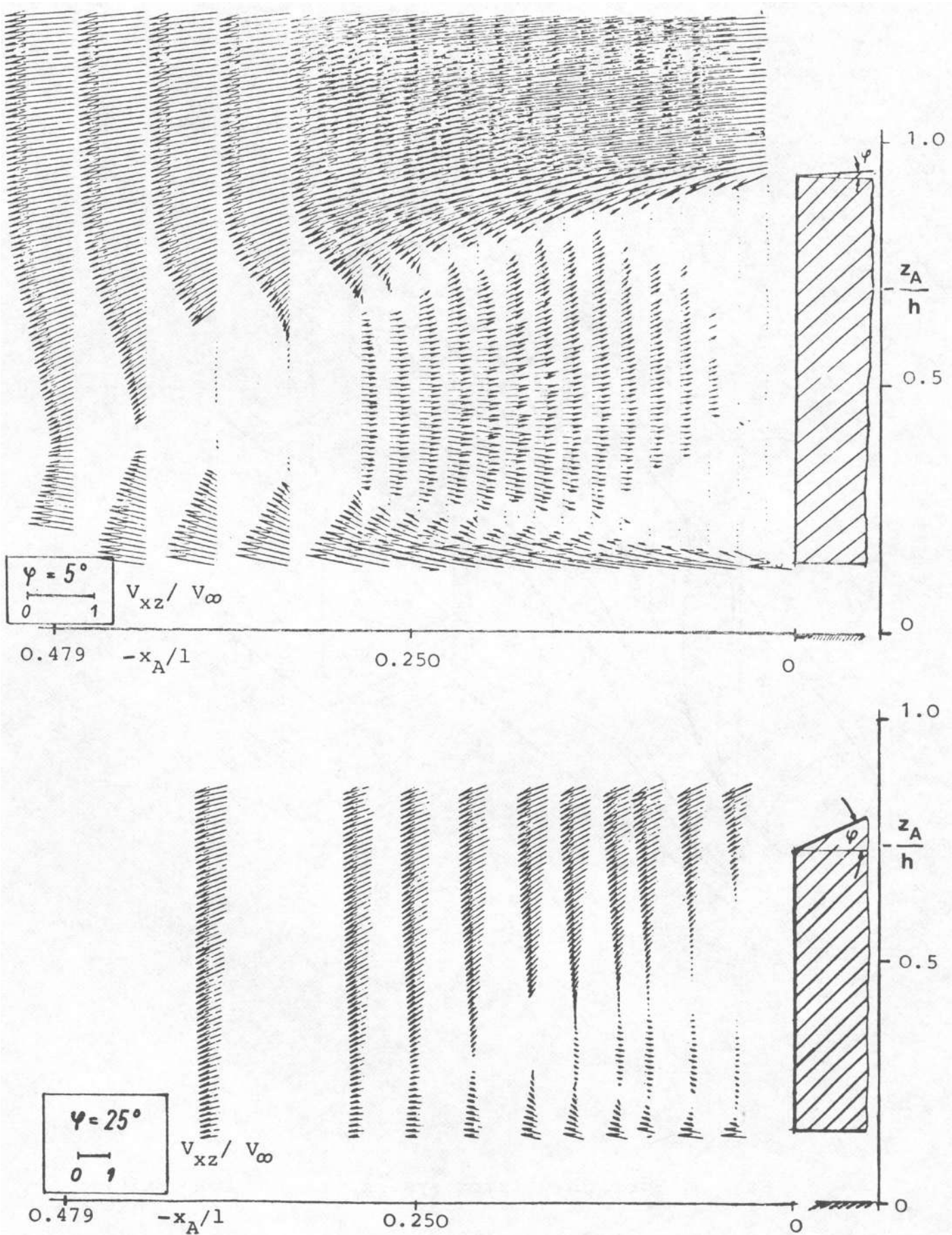


Fig. 7 Velocity distribution in wake central plane ( $\varphi = 5^\circ$  and  $25^\circ$ )

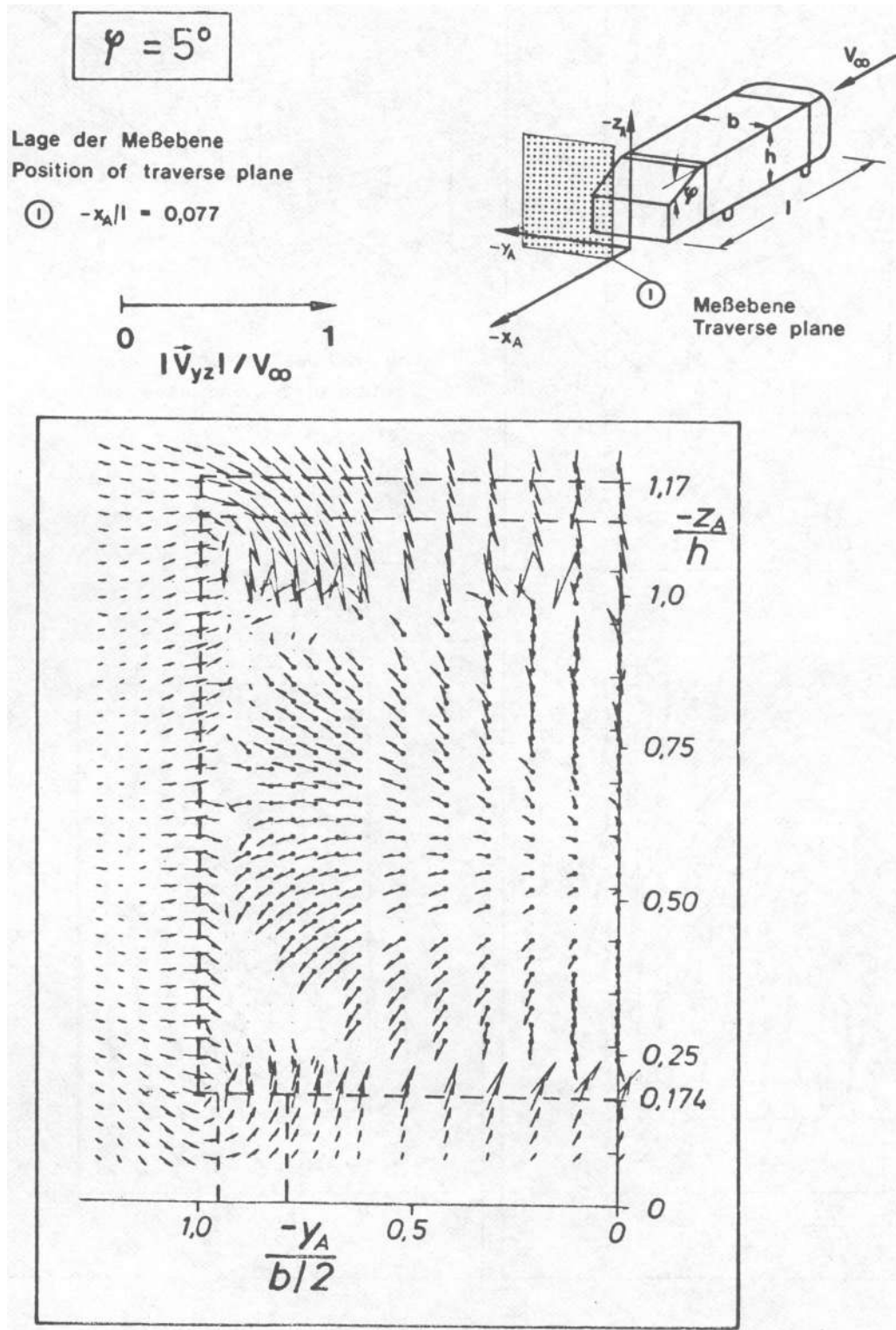


Fig. 8 Cross flow velocity field near model base ( $\varphi = 5^\circ$ )

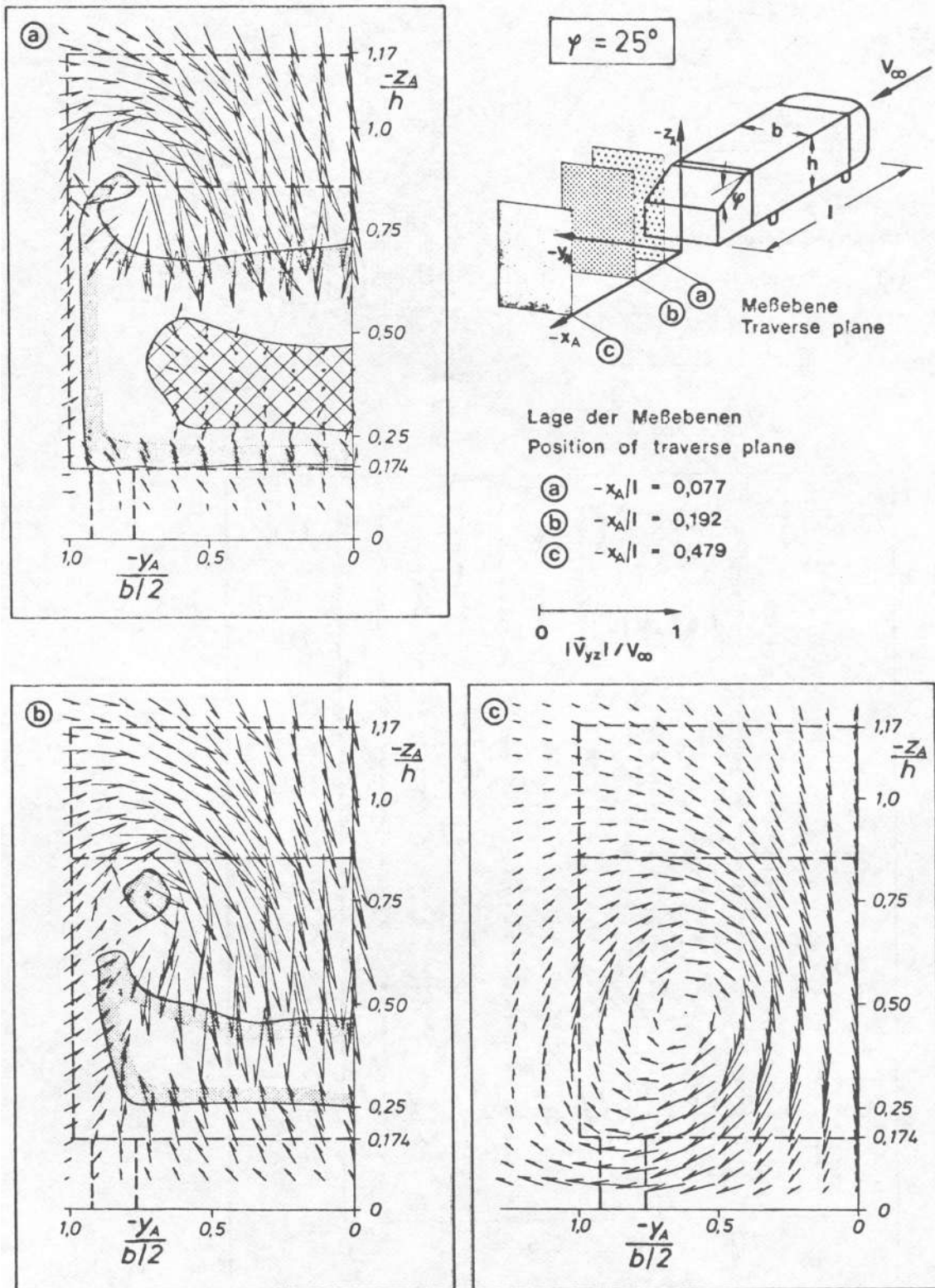


Fig. 9 Cross flow velocity distribution at three downstream stations in the wake ( $\varphi = 25^\circ$ )

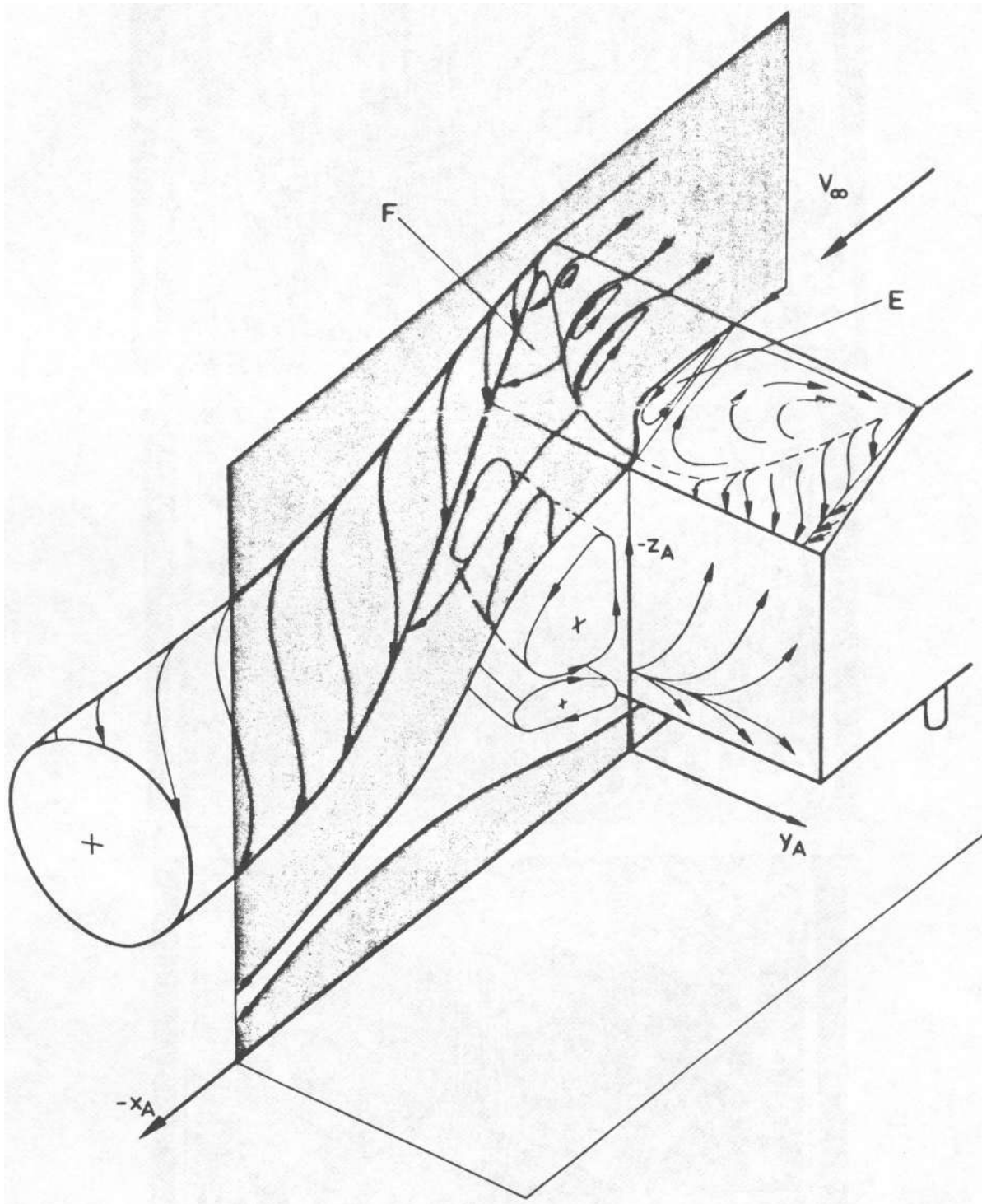


Fig. 10 Schematic representation of high drag flow ( $\varphi = 30^\circ$ )

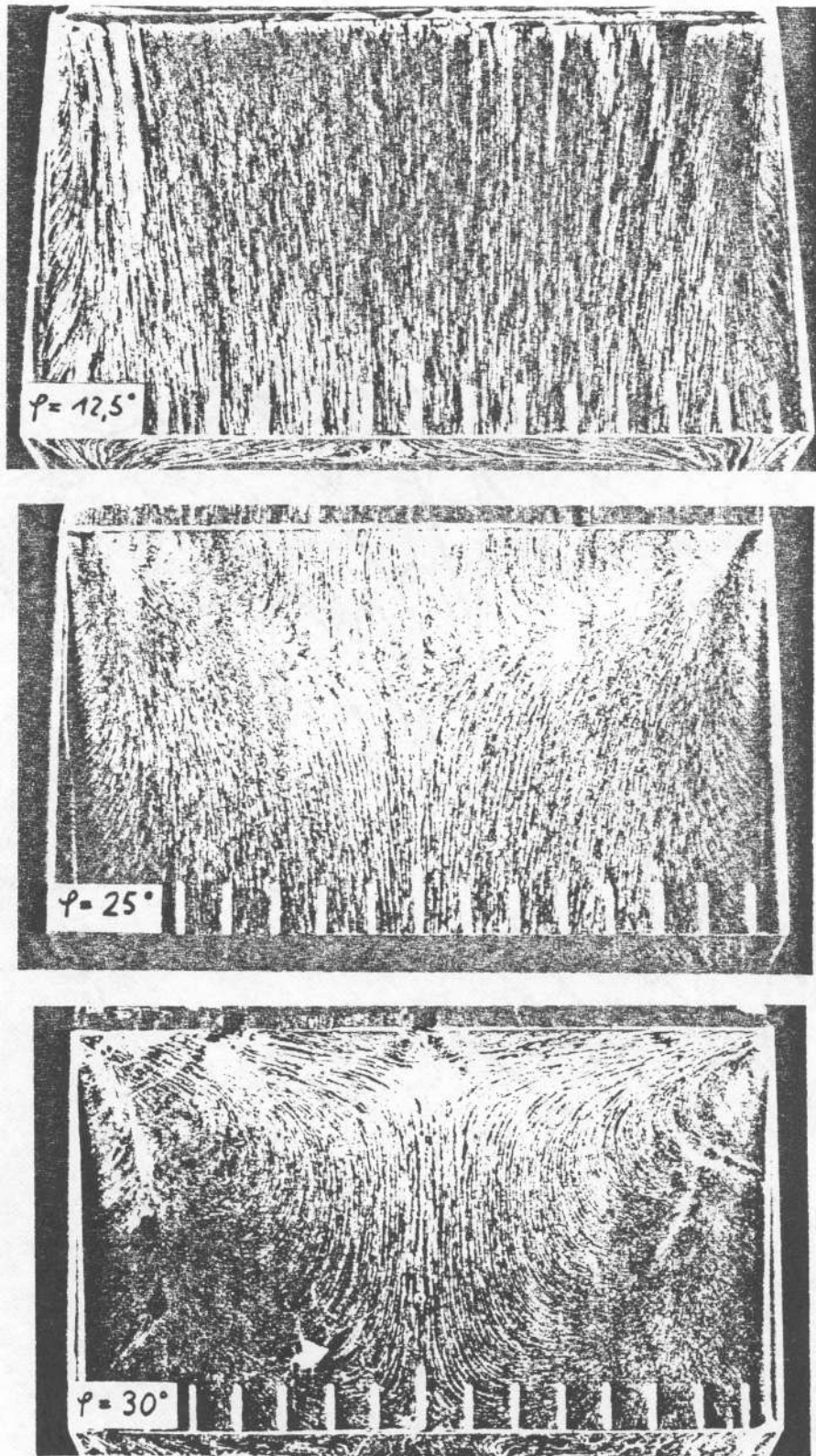
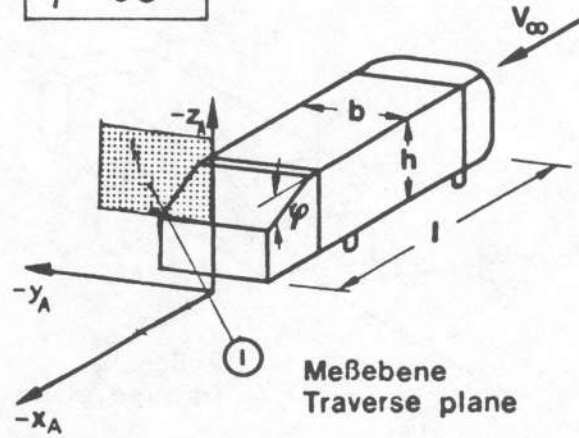


Fig. 11 Flow pattern on rear end slant surface

$\varphi = 30^\circ$



Lage der Meßebene  
Position of traverse plane

①  $-x_A/l = 0,0$

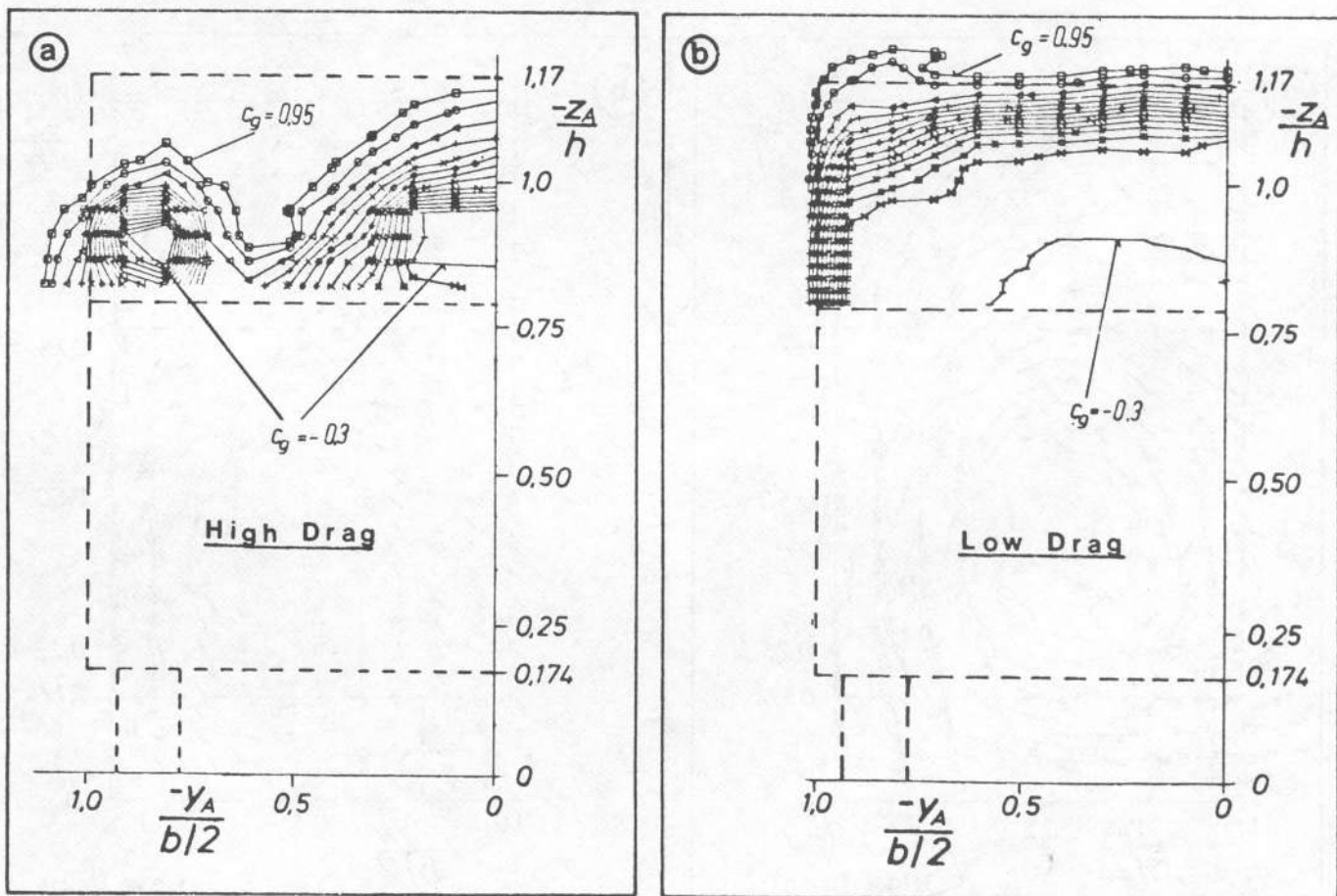
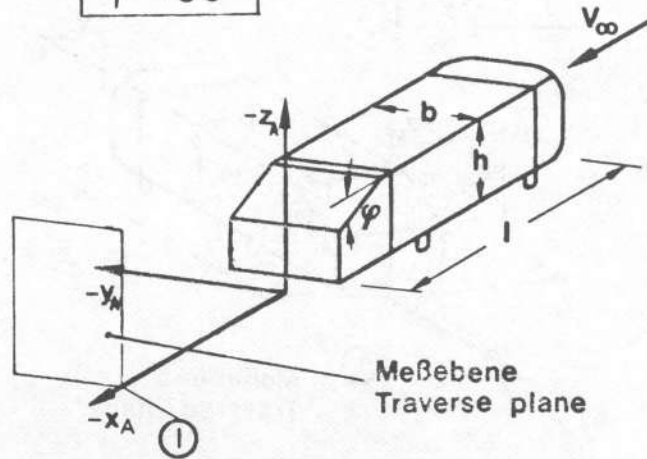


Fig. 12 Total pressure isobars above base edge. High drag and low drag flow ( $\varphi = 30^\circ$ )

$\varphi = 30^\circ$



Lage der Meßebene  
Position of traverse plane

①  $-x_A/l = 0,479$

$|\vec{V}_{yz}| / V_\infty$

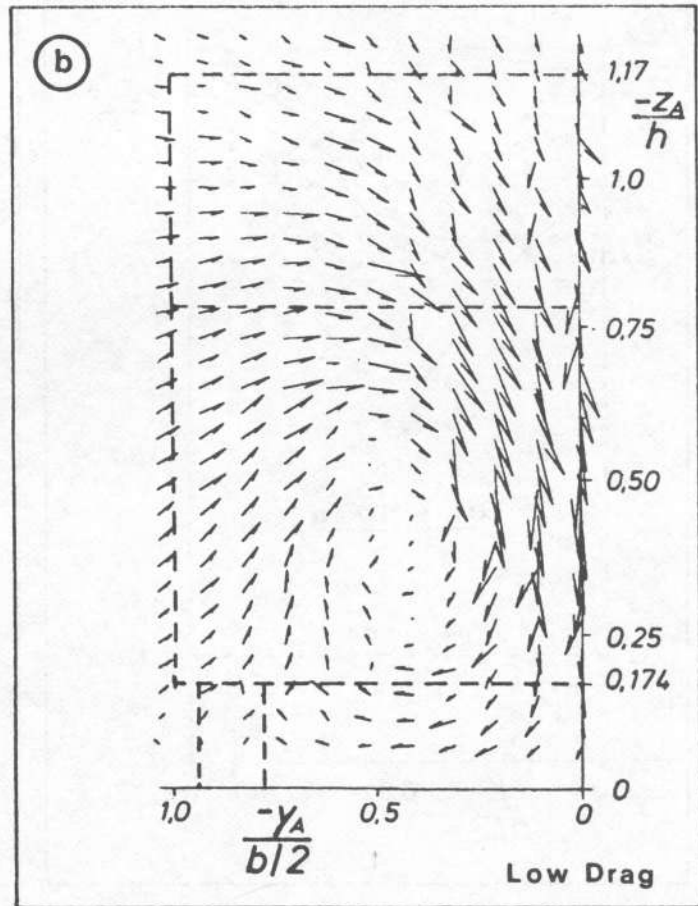
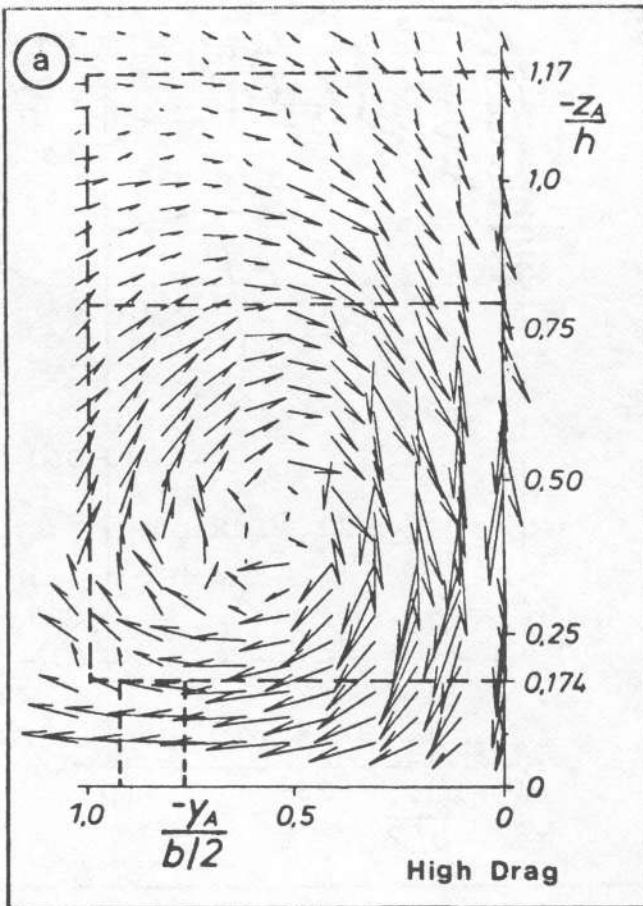


Fig. 13 Cross flow velocity distribution in far wake. High drag and low drag flow ( $\varphi = 30^\circ$ )

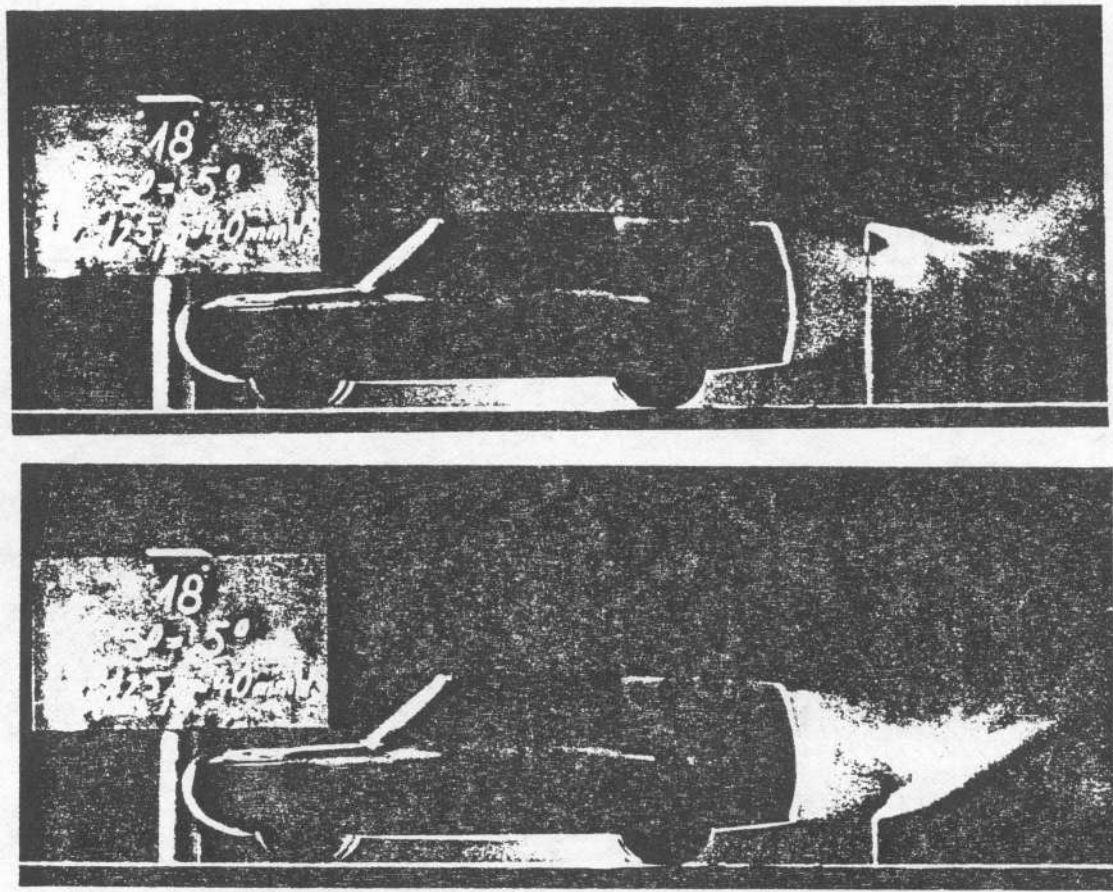


Fig. 14 Flow visualisation through smoke injection in wake central plane ( $\varphi = 5^\circ$ )

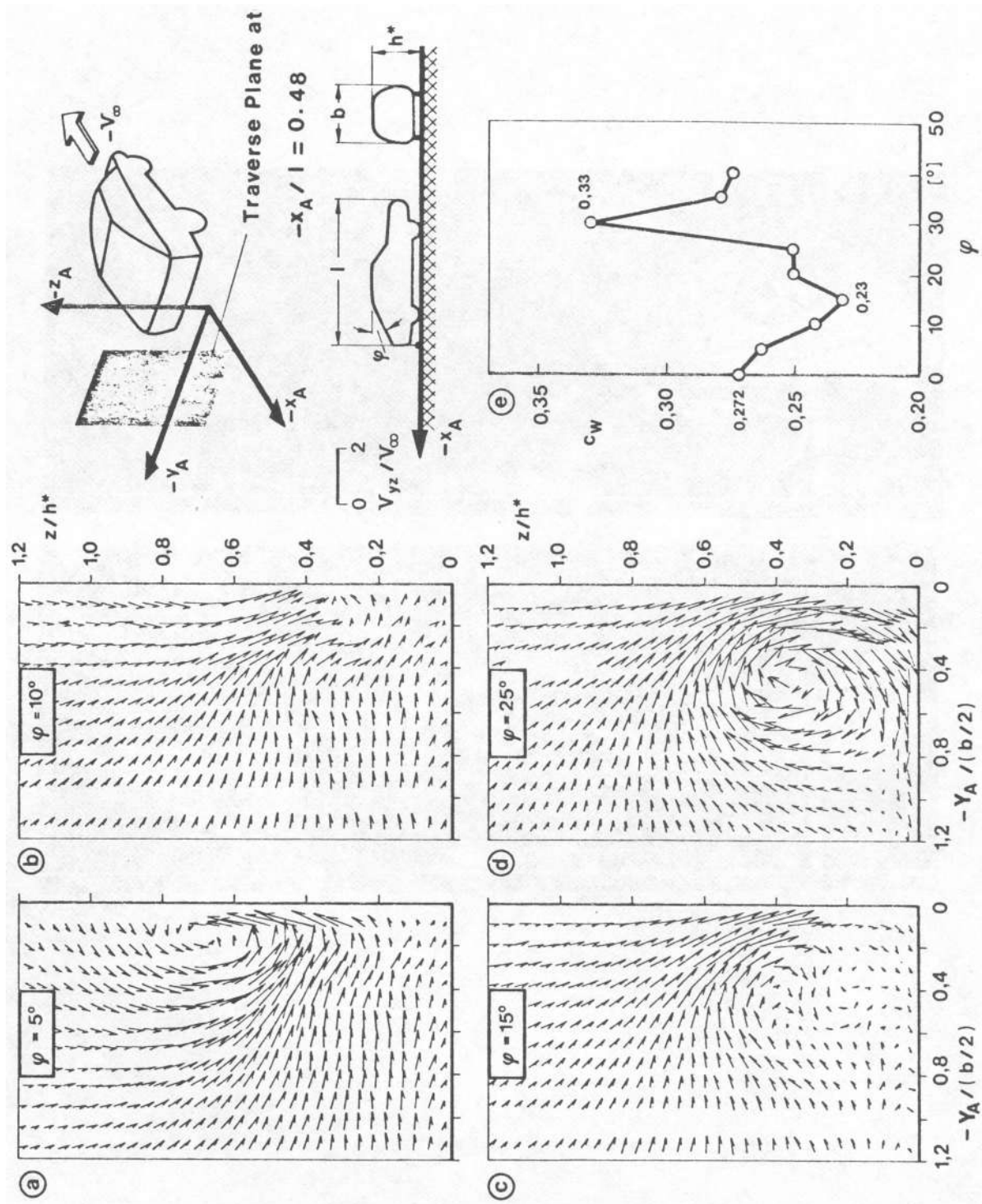
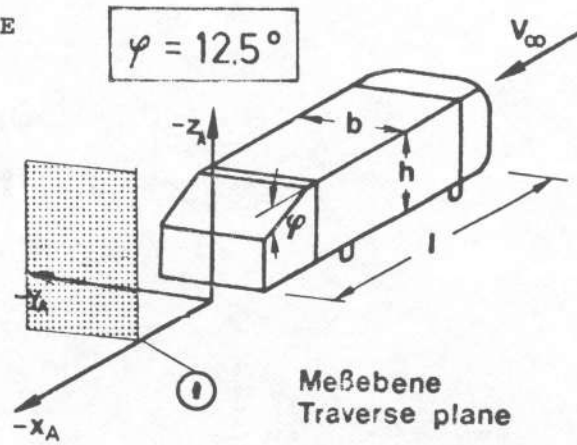


Fig. 15 (a,b,c,d) cross flow velocity distribution for different base slant angles  $\varphi$ , and (e) drag variation with  $\varphi$



Lage der Meßebene  
Position of traverse plane

①  $-x_A/l = 0,115$

$0 \rightarrow \frac{|\vec{V}_{yz}|}{V_\infty} \rightarrow 1$

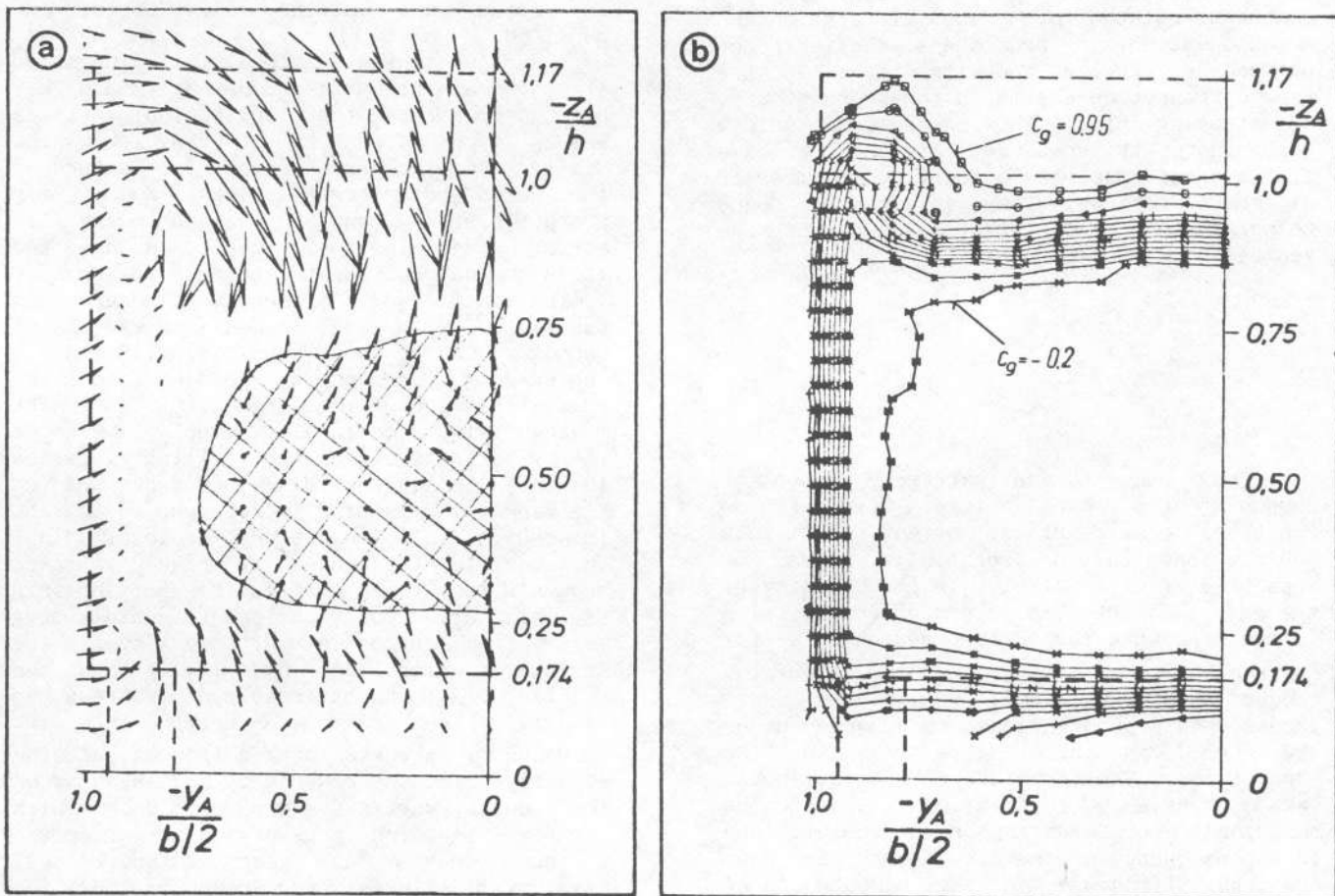


Fig. 16 Cross flow velocity distribution and isobars in wake of low drag configuration ( $\varphi = 12.5^\circ$ )